ACS APPLIED NANO MATERIALS

www.acsanm.org Article

Inorganic–Organic Interfacial Electronic Effects in Ligand-Passivated WO_{3-x} Nanoplatelets Induce Tunable Plasmonic Properties for Smart Windows

Jacob T. Lee,[§] Debabrata Das,[§] Gregory A. Davis, Jr., Sumon Hati, C. V. Ramana,* and Rajesh Sardar*

Cite This: *ACS Appl. Nano Mater.* 2022, 5, 9970–9980 Read Online

ACCESS | Metrics & More | Article Recommendations | Supporting Information

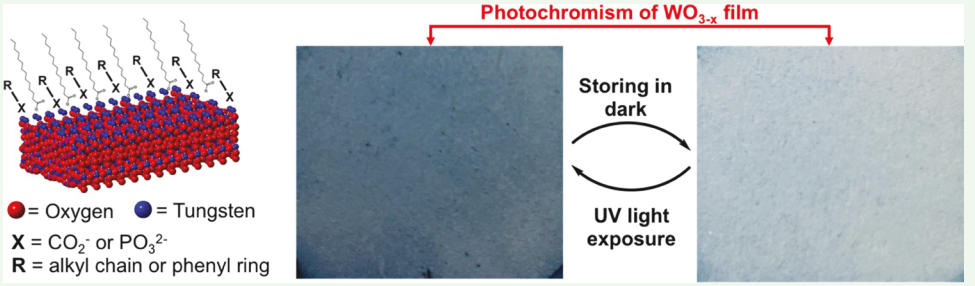

ABSTRACT: Transition-metal oxide (TMO) nanocrystals (NCs), displaying localized surface plasmon resonance (LSPR) properties, are an emerging class of nanomaterials due to their high stability, high earth abundance, and wide range of spectral responses covering the near-to-far infrared region of the solar spectrum. Although surface passivating ligands are ubiquitous to colloidal NC-based research, the role of ligands, specifically the impact of their chemical structure on the dielectric and LSPR properties of TMO NC films, has not been investigated in detail. Here, we report for the first time the chemical effects at the metal–ligand (inorganic–organic) interfaces influencing the optical constants and LSPR properties of thin films comprising highly oxygen-deficient, sub-stoichiometric, LSPR-active tungsten oxide (WO_{3-x}) nanoplatelets (NPLs). We studied ligands with two different types of binding head groups, aromatic conjugation, and short and long hydrocarbon chains. Using density functional theory calculations, we determine that the changes in the interfacial dipole moments and polarizability control the permittivity at the interface, resulting in the alteration of dielectric and LSPR properties of ligand-passivated NPL in thin nanocrystalline films. The photochromic properties of WO_{3-x} NPL passivated with different ligands in thin films have also been investigated to highlight the impact of interfacial permittivity caused by the chemical structures of passivating ligands. Taken together, this study provides a fundamental understanding of emerging properties at the metal–ligand interface that could be further optimized for energy efficiency in smart windows.

KEYWORDS: *plasmonic, tungsten oxide, nanoplatelets, surface chemistry, dipole moment, permittivity, photochromic*

INTRODUCTION

Colloidally synthesized transition-metal oxide (TMO) nanocrystals (NCs) have been extensively studied for their wide range of applications including electro- and photocatalysis, photovoltaics, sensors, and plasmonic and molecular electronic devices.[1−5] Furthermore, TMO NCs are also successfully implemented in electro- and photochromic device fabrication.[6] This wide-ranging expansion of the field is due to unique optoelectronic properties of TMO NCs that arise from large, polarizable metal–oxygen bonding and a strong correlation between the localized transition metal valence electrons.[7] Inorganic crystal defect engineering in TMO NCs further creates new properties, specifically oxygen vacancies generate free electrons in the conduction band that collectively oscillate upon the interaction with an incident electromagnetic field,[8] generating localized surface plasmon resonance (LSPR) properties. The LSPR properties of NCs are dependent on their free carrier concentrations, morphology, and the chemical structure of the ligands passivating the surface. Recent studies showed that chemical interactions between the surface-ligand and noble metal NC significantly influence the LSPR properties.[9−11] This is due to alteration in electronic states at the metal–ligand (inorganic–organic) hybrid interface. More specifically, chemically induced changes in the interfacial dipole moment and permittivity control the LSPR properties of ligand-passivated NCs. Considering the intrinsic benefits of

Received: May 20, 2022
Accepted: June 23, 2022
Published: July 6, 2022

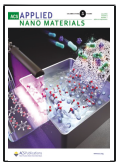

https://doi.org/10.1021/acsanm.2c02218
ACS Appl. Nano Mater. 2022, 5, 9970–9980

colloidal TMO NCs, the impact of chemical interactions at the interface between oxygen vacant NCs and passivating ligands on spectroscopic properties (e.g., real and imaginary portion of the dielectric function) has not been studied in detail. While the search for better and alternative materials to well-known plasmonic metals (Au, Ag) continues to be a challenging scientific problem, such fundamental exploration of the surface/interface interactions and structure−chemistry−property relationships are expected to provide excellent opportunities for the design and development of advanced optoelectronic devices such as energy-efficient smart windows and optical switches.

Since the first report,[12] pure and doped tungsten oxide (WO_3) thin films have been extensively studied for the fabrication of various electro- and photochromic, solid-state devices such as smart windows, flat-panel displays, electronic information displays, and optical memory.[13−18] Oxygen-deficient, sub-stoichiometric tungsten oxide (WO_{3-x}) can be obtained in various compositions,[19,20] and amongst them, thermodynamically stable, highly oxygen-deficient crystal structure $WO_{2.72}$ has attracted much attention due to the diverse optoelectronic properties and potential application in photo(electro) catalysis, gas sensing, and photochromatic systems.[18,21−25] Utilizing colloidal synthetic methods, oxygen-deficient WO_{3-x} NCs can be synthesized in various shapes such as rods and wires.[19,26,27] Colloidal WO_{3-x} NCs display shape-dependent plasmonic properties where the LSPR wavelength can be tuned in the near-infrared (NIR) to mid-infrared region of the solar spectrum which is an important range for applications including photodynamic therapies, telecommunications, and solar heat regulation.[28] Through the use of WO_{3-x} NCs, electro- and photochromic material-based smart windows can be developed to control building temperatures and light levels greatly decreasing overall energy consumption.[29] Recently, we developed a high-temperature colloidal method to synthesize ultrathin LSPR-active WO_{3-x} nanoplatelets (NPLs).[26] The LSPR wavelength of these NPLs can be tuned between 1200 and 1600 nm by controlling the oxygen deficiency, where a free electron concentration of 4.13×10^{22} cm^{-3} provided an LSPR peak position of ∼1200 nm. Furthermore, appropriate surface-ligand engineering provided additional means to increase free electron concentration (8.4×10^{22} cm^{-3}) and thus pushed the LSPR wavelength toward the visible region.[30] Together, ligand-induced alteration of free electrons in WO_{3-x} NCs is controlled by the interfacial chemical interaction between inorganic NC and organic ligands. In this context, the polarizability of the metal−ligand bond should govern the optoelectronic and dielectric properties of ligand-passivated WO_{3-x} NCs. Therefore, it is important to investigate the roles of surface passivating ligand at the inorganic−organic hybrid interface on the dielectric and LSPR properties to further optimize the performance of energy-efficient smart window applications. Although we have extensively investigated the dielectric properties of non-LSPR-active WO_3 thin films,[31] to the best of our knowledge, such investigation has not been conducted with LSPR-active WO_{3-x} NCs at this time.

In this article, using ultraviolet−visible−near-infrared (UV−vis−NIR) spectroscopy and spectroscopic ellipsometry, we investigate the influence of surface-ligand structural parameters (binding head group type and chain lengths) on the LSPR response and dielectric function of ligand-passivated WO_{3-x} NPL thin films. WO_{3-x} NPLs passivated with ligands containing a tridentate binding head group display a free electron density of (N_e) $2.5−3.0 \times 10^{22}$ cm^{-3} and an absorption coefficient of 8000−14 000 cm^{-1} in thin films. Our density functional theory (DFT) calculations show that the interfacial dipole moments and polarizability strongly depend on the chemical structure of the ligand that together influence the permittivity at the interface, and thus modulate the LSPR response of thin films. The theoretical presumption is further verified with spectroscopic ellipsometry measurements, which show a negative trend for the real optical permittivity. Importantly, it has been reported that photochromism in WO_3 occurs due to the presence of oxygen vacancies, therefore it is expected that highly oxygen-deficient and anisotropic WO_{3-x} NC thin films would display interesting photochromic behavior. Therefore, we study the photochromic response of WO_{3-x} NPL thin films to gain a fundamental understanding of the impact of ligands on photosensitivity.

RESULTS AND DISCUSSION

Fabrication and Characterization of LSPR-Active NPL Thin Films. Ultrathin WO_{3-x} NPLs were synthesized using our previously published procedure with slight modifications.[26] Briefly, tungsten (V) ethoxide was injected into a mixture of myristic acid (MA) and 1-octadecene under a N_2 atmosphere at 290 °C followed by the immediate injection of N_2 purged oleylamine (OLA). The color of the solution immediately turned blue indicating the formation of oxygen-deficient tungsten oxide NCs and the reaction was allowed to proceed for another 60 min. Next, the reaction mixture was cooled to 100 °C and transferred to an N_2 purged flask containing the ligand of choice as depicted in Scheme 1. The temperature of

Scheme 1. Representation of the (A) Ligand-Treated WO_{3-x} NPLs, (B) Thin-Film Fabrication of Purified NPLs, and (C) Chemical Structure of Ligands Used in the Study

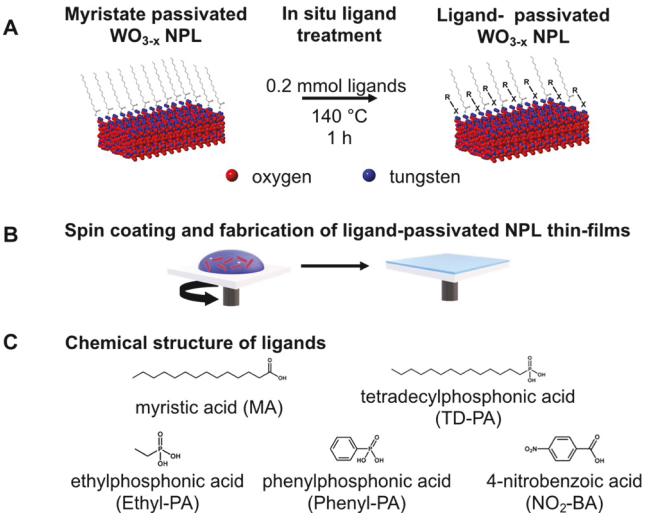

the reaction mixture containing NPLs and newly introduced ligands was raised to 140 °C and allowed to react for an additional 60 min under N_2. Additional information such as the concentration of ligands and treatment time are provided in the Experimental Section. Each ligand-treated sample was then dispersed in a 50:50 mixture of chloroform ($CHCl_3$) and toluene and spin coated on a 15 mm × 15 mm glass slide to produce nanoscale thin films.

https://doi.org/10.1021/acsanm.2c02218
ACS Appl. Nano Mater. 2022, 5, 9970−9980

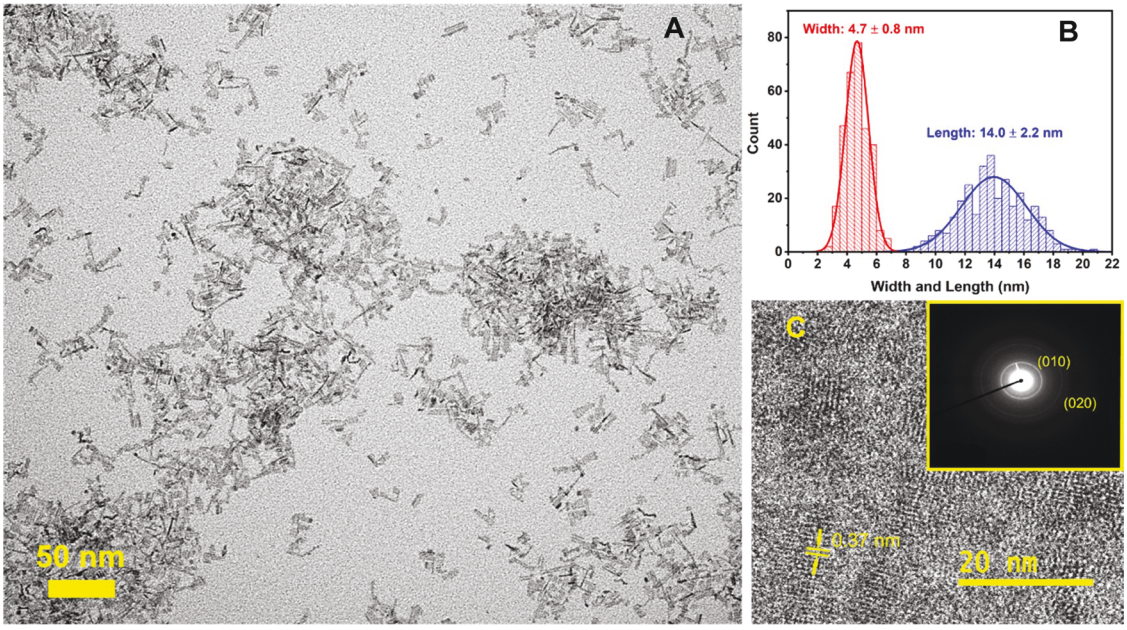

Figure 1. Representative low-magnification TEM image of WO_{3-x} NPLs (A), corresponding histogram of dimension analysis (B), and high-resolution TEM image showing lattice spacing and diffraction correspond to the WO_3 (010) plane (C).

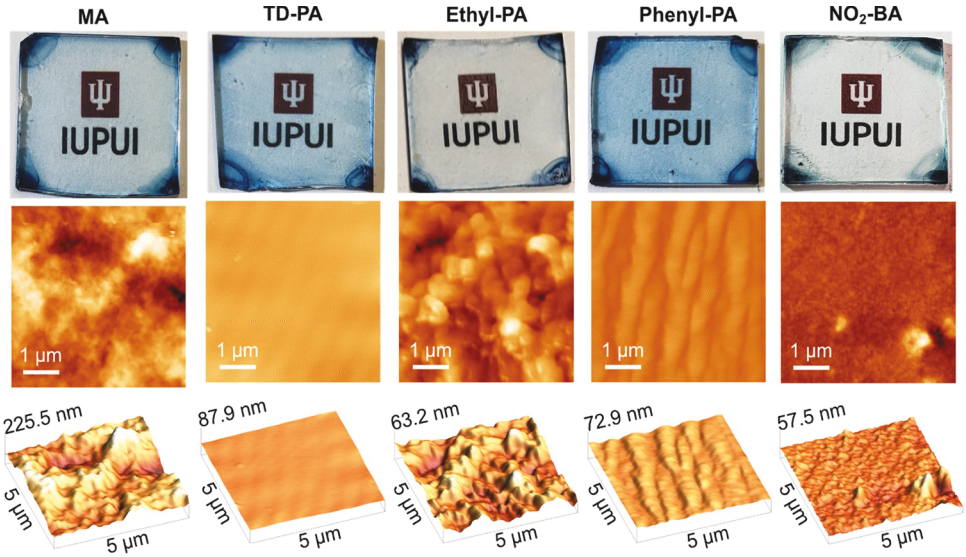

Figure 2. (Top row) Photographs of spin-coated films after undergoing ligand treatment to passivate the surface of NPLs with ligands listed at the top of each column. (Middle row) AFM images of each fabricated film. (Bottom row) Three-dimensional (3D) representation of the AFM film studied.

We should mention that the original WO_{3-x} NPLs are passivated by a mixture of MA and OLA.[26] To further explore the ligand effects on the LSPR properties of NPLs in thin films, we selected a variety of ligands based upon the binding ability of head groups and the chemical structure of their backbone. Herein, we used tetradecylphosphonic acid (TD-PA), ethylphosphonic acid (Ethyl-PA), phenylphosphonic acid (Phenyl-PA), and 4-nitrobenzoic acid (NO_2-BA). The phosphonate ($-PO_3^{2-}$) group of alkylphosphonic acids is known to form strong multidentate metal−phosphonate bonds both in macroscopic thin film and metal chalcogenide NCs.[32,33] We showed that TD-PA is a unique surface passivating ligand that not only increased the passivation sites per ligand compared to alkylcarboxylate ligands allowing greater passivation of under-coordinated near-neighbor tungsten atoms in highly deficient WO_{3-x} NPLs but also substantially improved the LSPR properties of colloidal WO_{3-x} NPLs.[30] Our selected ligands, Ethyl-PA, Phenyl-PA, and NO_2-BA provide a wide variety of structural diversity such as length of the alkyl chain, conjugation, and electron-withdrawing substitution. Colloidal synthesis and ligand exchange of WO_{3-x} NPLs, fabrication of thin films, and the chemical structure of ligands are shown in Scheme 1. These ligands can be categorized into three distinct groups: (1) long aliphatic chain ligands containing phosphonate ($-PO_3^{2-}$) and carboxylate ($-CO_2^-$) binding head groups (i.e., TD-PA and MA); (2) ligands with different backbones but an identical, $-PO_3^{2-}$ binding head group (i.e., TD-PA, Phenyl-PA, and Ethyl-PA); and (3) ligands with aromatic π-conjugation but two different binding head groups (i.e., NO_2-BA and Phenyl-PA). We believe that these three distinct

https://doi.org/10.1021/acsanm.2c02218
ACS Appl. Nano Mater. 2022, 5, 9970−9980

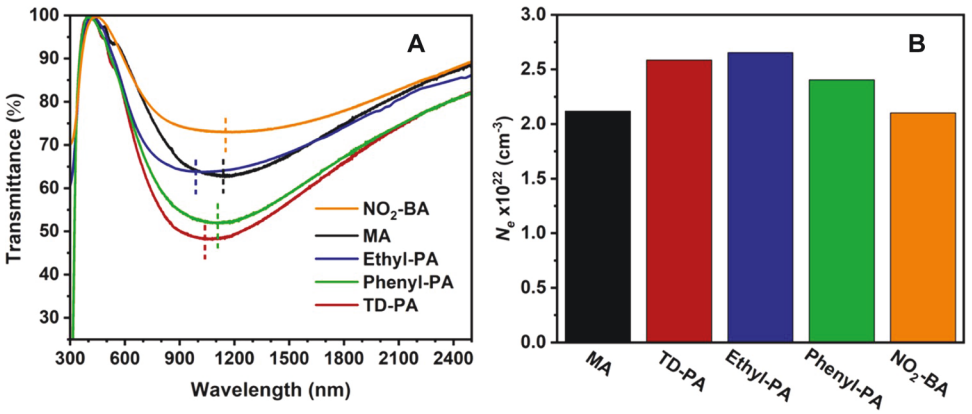

Figure 3. (A) UV−vis−NIR transmission spectra of fabricated films consisting of different ligand-passivated WO_{3-x} NPLs. (B) Calculated free carrier concentration (N_e) from thin-film optical data.

structural parameters of surface passivating ligands will influence the electronic properties at the metal−ligand interface of ligand-passivated WO_{3-x} NPLs, and thus are expected to alter the LSPR response of the fabricated thin films.

The dimensions of ligand-passivated WO_{3-x} NPLs were characterized by transmission electron microscopy (TEM). Figure 1A illustrates the TEM image of mixed MA/OLA passivated NPLs. The lateral dimensions of NPLs are determined to be ∼14 and 4.7 nm in length and width, respectively (Figure 1B,C). Based on our recent work,[30] we do not anticipate any morphological changes in the NPL during the ligand treatment. We used purified samples to prepare thin films. Spin coating of all ligand-treated WO_{3-x} NPL samples results in thin transparent films of varying blue hues (Figure 2). We performed atomic force microscopy (AFM) imaging to analyze the morphology of different ligand-passivated WO_{3-x} NPL films. As shown in Figure 2, surface passivation of NPLs with ligands of varying tail structures results in distinct surface topologies. Importantly, ligands containing phosphonic acid-binding head groups result in much smoother and packed films. We believe that the hydrophobic character of a long hydrocarbon chain of the TD-PA and phenyl ring of Phenyl-PA increases the solution dispersibility of ligand-passivated WO_{3-x} NPLs in a hydrophobic solvent, i.e., the chloroform−toluene mixture used for film preparation. Furthermore, superior surface charge neutrality due to the formation of tridentate W-phosphonate bonding could enhance the solution dispersibility and stability. In contrast, although Ethyl-PA contains a phosphonate binding head group, a very short ethylene tail does not provide adequate solution dispersibility and stability that result in inhomogeneous film formation. Finally, the hydrophobic character of the phenyl ring in NO_2-BA allows good film formation. All of these films were further characterized by scanning electron microscopy (SEM) (Figures S1−S5), which supports the AFM results. As shown in Figure 2, different ligands produce thin films with a distinct color intensity that required us to examine the optoelectronic properties of these thin films.

We performed UV−vis−NIR analysis to characterize the initial optoelectronic response of all fabricated thin films comprising different ligand-passivated WO_{3-x} NPLs (Figure 3A). The LSPR peak maximum (λ_{LSPR}) for MA-passivated NPL is located at 1142 nm in the transmission spectrum (Figure 3A). The λ_{LSPR} is blue-shifted for all phosphonic acid-containing ligands. The λ_{LSPR} for Ph-PA, TD-PA, and Ethyl-PA are 1123, 1042, and 1034 nm, respectively. In contrast, NO_2-BA-passivated NPLs show a slight red shift of the LSPR peak to 1169 nm in comparison to MA-passivated NPLs. The observed blue shift of the λ_{LSPR} upon passivation of WO_{3-x} NPLs with phosphonic acid ligands is in agreement with our previous work,[30] which is in part, due to the formation of multidentate W-phosphonate bonding that allows passivation of surface trap states. The formation of highly oxygen-deficient plasmonic WO_{3-x} causes a reduction event to occur where typical W^{+6} centers can be reduced to W^{+5} and even W^{+4} due to the presence of free electrons.[34] Additionally, the ultrathin nature of our WO_{3-x} NPLs results in a large percentage of oxygen atoms present on the surface facilitating a substantial amount of surface oxygen vacancies, which create shallow surface traps.[35,36] These surface traps caused by oxygen vacancies on W atoms can be successfully passivated with the tridentate binding phosphonate ($-PO_3^{2-}$) binding head group containing ligands compared to bidentate binding carboxylate ($-CO_2^-$) ligands.[30] Therefore, tridentate phosphonate-tungsten bonding provides stronger interactions than bidentate carboxylate-tungsten bonding. The increased surface passivation and stronger electronic interactions of phosphonate ligands stabilize surface W and prevent the transfer of the conduction band electrons to trap sites, thus increasing the free carrier density. This change in the λ_{LSPR} can be correlated to the free electron density (N_e) through the Drude−Lorentz model, which is a derivatization of the complex dielectric function of the material (eq 1).[37]

$$\varepsilon_\omega = \varepsilon_r + \varepsilon_i \tag{1}$$

where ε_ω is the dielectric of the material and ε_r and ε_i are the real and imaginary portions of the dielectric, respectively. It is important to note that the derivatizations of ε_ω are often used to describe optoelectronic phenomena and as such ε_r and ε_i are described throughout this article.

For the calculation of N_e, the application of the Drude model for bulk materials becomes,

$$\omega_{LSPR} = \sqrt{\frac{\omega_p^2}{\varepsilon_\infty - \varepsilon_r} - \gamma^2} \tag{2}$$

where ω_{LSPR} represents the LSPR frequency, ω_p the bulk plasma oscillation frequency of electrons, and ε_∞ the high-frequency dielectric constant, which is reported in the

https://doi.org/10.1021/acsanm.2c02218
ACS Appl. Nano Mater. 2022, 5, 9970−9980

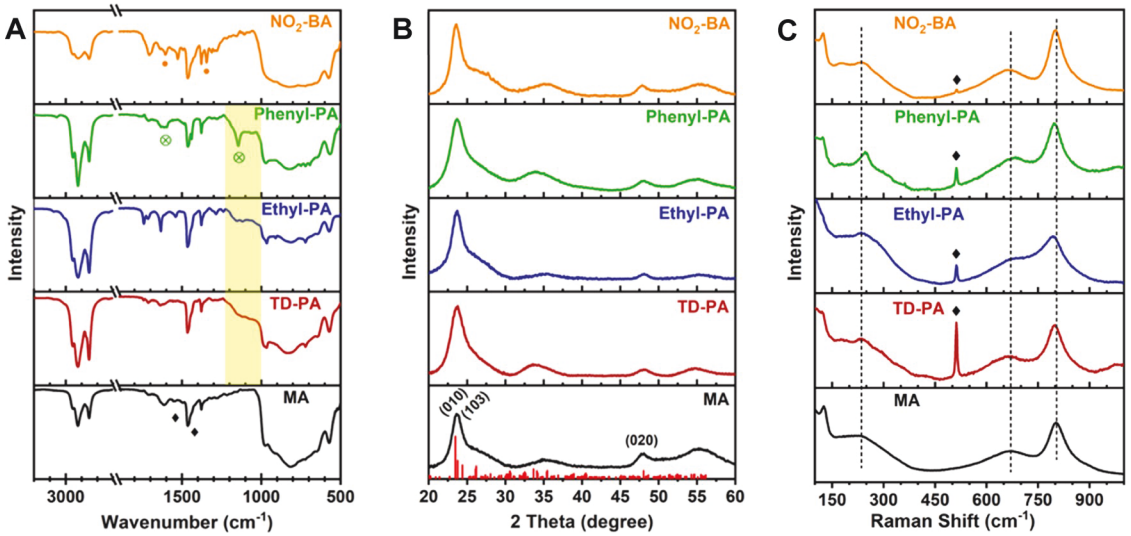

Figure 4. (A) FTIR spectra of various ligand-passivated NPLs. Black diamonds in the MA spectrum represent carbonyl-related stretching. Yellow shaded area in the three-phosphonate-containing NPLs represents the broad W-phosphonate bonding region. Green symbols in Phenyl-PA represent the peaks related to arylphosphonate-specific vibrations. Orange dots of NO_2-BA represent nitro and aromatic-related vibrations. (B) Experimental X-ray diffraction (XRD) patterns of each ligand-passivated NPL thin films. The monoclinic $WO_{2.72}$ standard has been included as a reference (vertical red lines, PDF #71-2450). Major diffraction planes (010), (103), and (020) are labeled in the MA sample and are present in all other samples. (C) Raman spectra of each ligand-passivated NPL thin film. Black diamonds represent the stretching mode related to the silicon substrate. Black dashed lines highlight WO_{3-x}-related vibrations and are present in all samples.

literature for tungsten oxide as 4.8.[38] The real part of the complex dielectric function of plasmonic nanostructures can be calculated by eq 3 through an oblate spheroid structure shape factor, κ, to model our NPL[26] and the bulk refractive index of the surrounding medium, ε_m, which is 1.0 for air in our film application.

$$\varepsilon_r = -\kappa\varepsilon_m \tag{3}$$

The bulk collision frequency, γ, is calculated through Lorentz fitting of the NIR spectra and represents the damping of the oscillation of the electrons. Thus, ω_p is dependent upon N_e as

$$\omega_p^2 = \frac{N_e e^2}{\varepsilon_0 m_e} \tag{4}$$

where m_e is the effective mass of an electron in tungsten oxide ($1.2m_0$)[19] and m_0 is the rest mass of an electron. Our NPL-specific spectroscopic values used to calculate the N_e for different ligand-passivated NPL thin films are listed in Table S1. As shown in Figure 3B, N_e values for MA, TD-PA, Ethyl-PA, Phenyl-PA, and NO_2-BA are 2.12, 2.59, 2.65, 2.40, and 2.10×10^{22} cm^{-3}, respectively. Although the LSPR properties and N_e values of colloidal WO_{3-x} NCs have been reported in the literature,[19,26,27] to the best of our knowledge, this is the first example where N_e values of anisotropic shaped NCs are calculated for LSPR-active thin films. It has been observed in the literature that increased N_e can have a beneficial effect on the photochromic properties of solid-state devices.[39]

Confirmation of successful ligand passivation of WO_{3-x} NPLs was determined by Fourier transform infrared spectroscopy (FTIR) and the resulting spectra are shown in Figure 4A. Beginning with MA (black) at the bottom, bidentate-bound carboxylate passivation is signified by black dots at 1548 cm^{-1} representing asymmetric stretching and a shoulder at 1435 cm^{-1} for symmetric stretching of the carbonyl bond.[40] The sharp peak at 1466 cm^{-1} appears due to $-CH_2-$ vibrations from the ligand backbone.[41] W-Phosphonate bonding is confirmed in TD-PA (red), Ethyl-PA (blue), and Phenyl-PA (green) by the appearance of peaks located in the shaded area (1000−1230 cm^{-1}).[42,43] The presence of broad peaks for TD-PA and Ethyl-PA is indicative of tridentate phosphonate binding modes. The sharp W-arylphosphonate stretch of Phenyl-PA appears at 1148 cm^{-1}.[41] The presence of an aromatic backbone in Phenyl-PA is further confirmed by the sharp −C = C− stretching of the phenyl ring at ∼1600 cm^{-1}. This same stretching vibration is also present in NO_2-BA (orange, top) along with the −N═O stretch at 1347 cm^{-1} (orange dots).[41]

The crystal structure of all ligand-passivated WO_{3-x} NPLs was characterized by X-ray diffraction (XRD) and Raman spectroscopy to verify that no structural changes occurred during the ligand treatment process. As shown in Figure 4B, the XRD diffraction pattern of MA-passivated NPLs (black, bottom) shows peaks at ∼23.5 and ∼47.9° 2θ, respectively, which are related to (010) and (020) planes. Strong diffraction signatures suggest preferential growth in the (010) direction of monoclinic $WO_{2.72}$ NPLs.[44] The peak at 23.7° related to the (103) plane, which is also a known crystallographic shear plane of monoclinic $WO_{2.72}$, is distinguishable. We believe this plane mostly resides at the surface of our NPLs.[45] Overall, none of the diffraction patterns of the ligand-treated samples display any new or shifted characteristic peaks, and they all match well with the calculated monoclinic $WO_{2.72}$ standard (red lines) PDF #71-2450. Structural analysis by Raman provides similar results indicating no change in ligand treatment (Figure 4C). All ligand-treated samples contain characteristic oxygen-deficient crystal lattice vibration-related peaks, marked by dashed lines at 803, 668, and 233 cm^{-1}.[46−48] Raman spectroscopy is known to be sensitive to subtle surface binding changes and the position of Raman vibrational stretches could vary depending on the sampling deposition technique. As illustrated in Figure 4C, depending on the type of ligand used to passivate the surface of WO_{3-x} NPLs, we observe a slight

https://doi.org/10.1021/acsanm.2c02218
ACS Appl. Nano Mater. 2022, 5, 9970−9980

shift in the peak position in Raman spectra, which can be attributed to the changes in the film morphology, as well as electronic interactions between ligands and NPLs.[35,49] As described above, we showed that phosphonate and carboxylate binding head groups form different bonding interactions with WO_{3-x} NPLs. Therefore, we would expect slight variations in the Raman stretches depending on whether the ligands contain phosphonate or carboxylate binding head groups. Nevertheless, our in-depth structural analyses unequivocally support the presence of the bound ligand of choice on the surface of WO_{3-x} NPLs and they maintained good structural integrity without any remarkable changes. Importantly, fabrication and characterization of nanocrystalline thin films of WO_{3-x} NPLs highlight the importance of surface-ligand choice on the manipulation of their λ_{LSPR} position and subsequent change in N_e values upon passivation with ligands containing different chemical structures. It is crucial to highlight that our WO_{3-x} NPLs are ultrathin in nature and thus most of the atoms are at the surface. Under such circumstances, the surface structure would dictate the optoelectronic properties of NPLs. In this context, we could predict that any change in the electronic character of surface passivating ligands would influence the electronic structure at metal−ligand interface and thus the dielectric function. Therefore, it is crucial to further investigate the optoelectronic response of our ligand-passivated WO_{3-x} NPLs.

Investigating Ligand Effect on Optoelectronic Properties. Although we reported λ_{LSPR} values from the transmission data of our films, they do not account for the film thickness, which can vary even under identical deposition conditions due to the differences in solubility and assembly caused by the chemical structure of ligands. Figure 5 reports

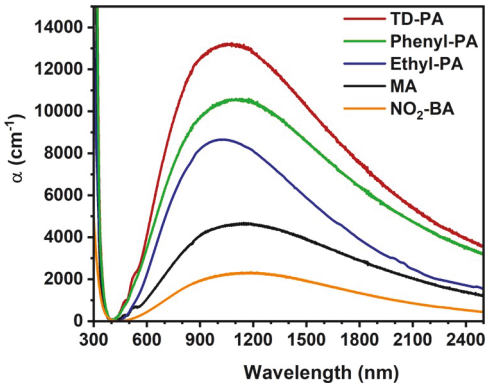

Figure 5. Plot of absorption coefficients vs wavelength for different ligand-passivated WO_{3-x} NPL thin films.

the calculated absorption coefficient (α) of all films using the cross-sectional thickness. The film thickness was determined using Image J analysis of SEM cross-sections of spin-coated films on 15 mm × 15 mm silicon substrates under identical parameters, see Figures S6−S10 for SEM cross-sectional images. The α values of NO_2-BA-, MA-, Ethyl-PA-, Phenyl-PA-, and TD-PA-passivated WO_{3-x} NPL films are 2320, 4705, 8650, 10 555, and 13 260 cm^{-1}, respectively. It is evident that the use of phosphonic acid-containing ligands increases the α value and can be qualitatively attributed to the increase in passivation caused by multidentate metal−phosphonate bonding. Although the bonding characteristic of TD-PA, Ethyl-PA, and Phenyl-PA are very similar, their chemical structures are quite different. Herein, we test the hypothesis that a change in dielectrics at the inorganic−organic hybrid interface, which originates from the chemical structure of ligands, impacts the intensity of the absorption, as well as the peak position. Until now, the structural impacts of ligands on LSPR-active plasmonic metal oxide NCs have not been studied.

In plasmonic WO_{3-x} NPLs, the Fermi level is close to the conduction band.[37,50] Therefore, any modulation in the electron density due to ligand binding and/or the permanent dipole moment (μ_P) of passivating ligands may change the polarizability (σ_P) at the metal−ligand interface resulting in changes in the optoelectronic response. Recently, Saito et al. reported that the change in chemically induced permittivity (CIP) caused by surface ligands can alter the optoelectronic response, specifically, increasing the LSPR peak intensity of Ag NC films.[51] We used the Langevin−Debye formula to deconvolute the relationship between interfacial dipole moment and permittivity of ligand-passivated NPLs to qualitatively describe the CIP effect in our WO_{3-x} NPL system (eq 5).

$$\frac{\varepsilon_r - 1}{\varepsilon_r + 2} = \rho_N \left(\frac{\sigma_P + \frac{\mu_P^2}{3k_BT}}{3\varepsilon_0} \right) \tag{5}$$

where ρ_N represents the molecular number density. In a very simplistic way, an increase in the right-hand bracketed term represents an increase in overall permittivity. We performed density functional theory (DFT) calculations of a small W-ligand cluster to determine the μ_p and σ values (see Figures S11−15) where carboxylate and phosphonate groups form bidentate and tridentate bonding with W sites, respectively. These different modes of bonding are expected to impact the interfacial dipole moment and permittivity. Table 1 compiles the μ_P, σ, and the term $\frac{\sigma_P + \frac{\mu_P^2}{3K_BT}}{3\varepsilon_0}$ of different ligand-W complexes.

Table 1. DFT-Calculated Dipole Moment and Polarizability of Passivating Ligands with Covalently Attached W Atoms

ligand	μ_P (D)	μ_P (C·m)	σ_P (C·m^2·V^{-1})	$\frac{\sigma_P + {\mu_P}^2 / 3k_BT}{3\varepsilon_0}$
TD-PA	16.2359	54.2×10^{-30}	58.1×10^{-40}	91.7×10^{-28}
Phenyl-PA	8.6373	28.8×10^{-30}	40.1×10^{-40}	26.8×10^{-28}
Ethyl-PA	6.4721	21.6×10^{-30}	32.2×10^{-40}	15.4×10^{-28}
MA	6.9967	23.3×10^{-30}	38.2×10^{-40}	18.1×10^{-28}
NO_2-BA	2.9120	9.71×10^{-30}	26.3×10^{-40}	3.87×10^{-28}

The bracketed values on the right-hand side for the five ligands that we studied maintain the following increasing order: NO_2-BA > Ethyl-PA > MA > Phenyl-PA > TD-PA. Except for Ethyl-PA, the permittivity trend is in agreement with the increase in α values observed in Figure 5. Among all ligands, the binding energy between W and carboxylate in NO_2-BA is the lowest because the W−O interface has the largest ionic bonding property due to the presence of an electron-withdrawing $-NO_2$ group at the para-position in the phenyl ring. In contrast, the long hydrocarbon tail of TD-PA possesses an electron-donating character that lowers the ionic bonding property at the W−O interface of TD-PA-passivated

https://doi.org/10.1021/acsanm.2c02218
ACS Appl. Nano Mater. 2022, 5, 9970−9980

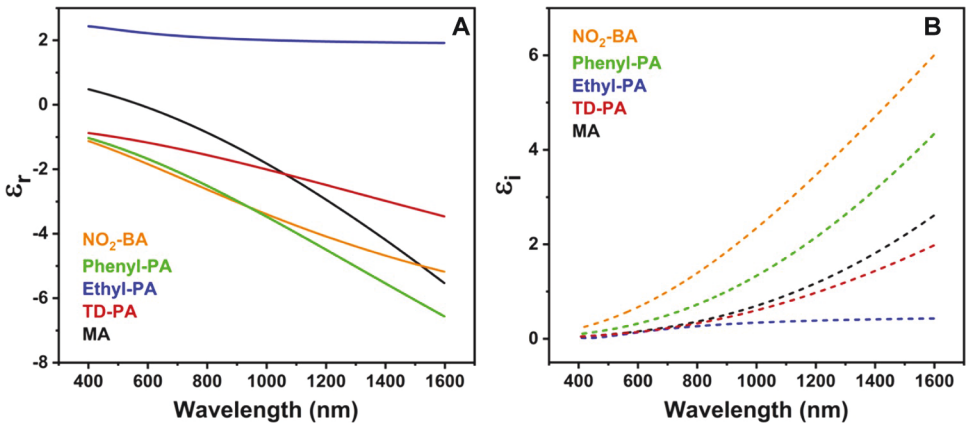

Figure 6. Real (A) and imaginary (B) parts of the complex dielectric functions determined from ellipsometry measurements of different ligand-passivated WO_{3-x} NPL thin films.

WO_{3-x} NPLs. Therefore, one could imagine an enhanced covalent bonding character at the W-ligand interface in TD-PA compared to NO_2-BA. The increase in interfacial covalent bonding would enhance the scattering rate of free conduction electrons of WO_{3-x} NPLs, resulting in higher LSPR peak intensity. Surprisingly, Ethyl-PA does not follow the experimentally determined α value and DFT-calculated $\left(\sigma_P + \frac{\mu_P^2}{3K_BT}\right)/3\varepsilon_0$. We believe that the induced dipole moment at the metal−ligand interface also influences the σ_P and thus the bracketed right-hand-side value in eq 5.[51] Therefore, we determined the induced dipole moment from first-principles calculations[52] and the values for different ligands are listed in Table S2. Indeed, the experimentally determined absorption coefficient values perfectly match the induced dipole moment. Together, experimental and theoretical results presented in Figure 5 and Tables 1 and S2, respectively, suggest that all five ligands interact differently with the W sites in WO_{3-x} NPLs. The higher induced and permanent dipole moments of the W-phosphonate system in comparison to the W-carboxylate unit cause higher permittivity in the former. It is also important to mention that the CIP effect should also alter the density of states at the organic−inorganic hybrid interface; however, performing such complicated calculations are beyond the scope of this article. Nevertheless, CIP effects should be taken into consideration for any ligand-passivated, organic−inorganic hybrid LSPR-active NC systems regardless of their chemical composition of inorganic counterparts.

To further investigate the CIP effects on LSPR properties of different ligand-passivated WO_{3-x} NPLs and to gain a deeper understanding of their optical/optoelectronic properties, we performed spectroscopic ellipsometry characterizations of all five ligand-passivated thin films to analyze the ε_r and ε_i portions of the dielectric function. The Drude dispersion model provided good fits (>99%) for all samples except for Ethyl-PA, which was a fit to the Cauchy dispersion formula (>99%). Ethyl-PA shows only positive values for ε_r and a little increase in ε_i, Figure 6A,B, respectively. It is likely that the poor stability of short-chain Ethyl-PA samples results in a lack of LSPR-active electrons. As shown in Figure 6A, four other samples are showing a gradual negative trend of the real part of the dielectric function, which confirms the existence of a strong LSPR response in those ligand-passivated WO_{3-x} NPL thin films.[53] Figure 6B presents the imaginary portion of the dielectric with even more positive values for all but Ethyl-PA signifying the differences arising from the surface−ligand interactions with the WO_{3-x} NPL films. Also, the trend noted in Figure 6B signifies the higher conductivity of electrons oscillating in the LSPR response.[51] Not unexpectedly, the highest values are obtained for NPLs treated with aromatic groups that provide a greater effective mean-free path allowing the wave function of free electrons to extend into molecular orbitals of the attached ligands through interfacial hybrid orbitals.[51] After in-depth analyses related to the structure and properties, it is imperative to further validate the potential of these materials in practical applications. For this purpose, we performed the photochromic performance evaluation of all of these ligand-passivated WO_{3-x} NPL thin films as discussed below.

Ligand Controlled Photochromic Response. Photochromism, the reversible change in coloration of the material upon light irradiation, is an important intrinsic property of tungsten oxide materials that have shown applications in smart windows and textiles.[6] The overall optical contrast and photochromic performance have been linked to changes in the crystal structure (i.e., cubic, hexagonal, and monoclinic), particle size, and morphology. Importantly, an increase in the specific surface area exhibits better photoreactivity in thin films.[54,55] However, most of these studies utilized tungsten trioxide (WO_3) materials.[6,54,56] It has been reported that photochromism in tungsten oxide occurs due to the presence of oxygen vacancies.[54] In this context, to the best of our knowledge, no photochromic studies are known in the literature utilizing highly oxygen-deficient, strong LSPR-active, anisotropically shaped WO_{3-x} NCs. More importantly, the results presented above show a strong ligand dependency on LSPR and dielectric properties of WO_{3-x} NPLs. To fill this gap, as a proof of concept, we studied the photosensitivity of highly deficient and anisotropic WO_{3-x} thin films as a function of surface passivating ligands. First, fabricated thin films of ligand-treated WO_{3-x} NPLs were exposed to 370 nm wavelength UV-LED light and then transferred to a spectrophotometer in a dark environment. Next, time-dependent LSPR spectra were collected to determine the peak intensity. As shown in Figure 7, we observe a steady decay of the LSPR peak intensity over time (Figure S16). It is known that the LSPR peak intensity of vacancy-doped metal oxides is dependent on the free carrier concentrations.[37] By correlating decay as a percentage of the initial post irradiation peak

https://doi.org/10.1021/acsanm.2c02218
ACS Appl. Nano Mater. 2022, 5, 9970−9980

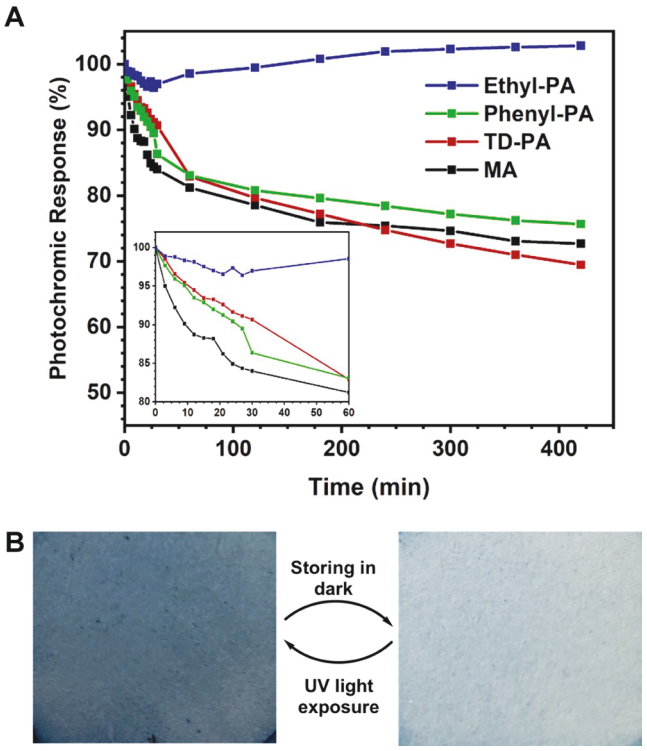

Figure 7. (A) Photochromic response of films obtained by UV irradiation for 5 min followed by acquisition of UV−vis−NIR spectra periodically. Samples were left in the spectrophotometer throughout the analyses. The inset shows the expanded photochromic response during the first 60 min of the study. (B) Photographs showing spin-coated, MA-passivated WO_{3-x} NPL films after 5 min of UV light irradiation (top) and after 8 h of optical measurements (bottom). Images were taken at the normal laboratory temperature.

intensity, we can better understand the photochromic characteristics of WO_{3-x} NPL thin films.

Ethyl-PA films very clearly have little photochromic effect, which is expected considering the overall instability of these films as supported by ellipsometry data. We should also mention that the NO_2-BA-passivated WO_{3-x} NPL film was unstable during UV light irradiation. This could be due to the lack of stability of W−O bonds arising from the electron-withdrawing $-NO_2$ group attached to the phenyl ring. This stability issue possibly leads to immediate oxidation of tungsten centers, resulting in fast decomposition of the film. Nevertheless, thin films comprising Phenyl-PA-, MA- and TD-PA-passivated WO_{3-x} NPLs display nearly identical responses where the TD-PA ligand displays the greatest change in the photochromic response. The first 60 min of the analysis presents some interesting data, specifically TD-PA-passivated WO_{3-x} NPL films display the slowest photochromic decay followed by Phenyl-PA and then MA. We hypothesize that this is due to a combination of the enhanced surface passivation of NPLs through multidentate phosphonate bonding and the increased permittivity of the material. It has been shown that photochromism in tungsten oxides occurs due to redox-active W^{+5}/W^{+6} chemistry in conjunction with adsorbed water as a hole scavenger.[57,58] Alternatively, wavefunctions of photo-excited holes can be delocalized to the ligand backbone through interfacial hybrid orbitals, thus reducing the timescale for electron−hole recombinations.[59,60] Furthermore, an increase in permittivity of the material resulting from a higher dipole moment enables better separation of photoexcited electrons and holes. Therefore, the electron−hole recombination would be much slower. An increase in surface passivation with suitable ligands should reduce the rate of W^{+5}/W^{+6} chemistry necessary for the reversible photochromic/bleaching process. Taken together, our results suggest that TD-PA passivated, LSPR-active WO_{3-x} NPL thin films could be an effective photochromic material for the fabrication of smart windows for energy-efficient architectures such as buildings and automobiles, as well as writing−reading−erasing devices.[6,29,61] While the structure−property evaluation of the ligand-passivated WO_{3-x} NPL thin films is encouraging, our future studies will focus on the multilayered device stack and interfacial effects for the optimization of the materials for direct integration into energy-efficient smart window applications.

CONCLUSIONS

In summary, we have reported the effect of the chemical structure of surface passivating ligands in modulation of optoelectronic properties of thin films comprising LSPR-active WO_{3-x} NPLs. Our in-depth spectroscopic characterizations unequivocally support the chemical attachment of surface passivating ligands onto the NPL surface. We have observed that the absorption coefficient of different films is strongly controlled by the chemical structure of surface passivating ligands. Our theoretical calculations support the mechanism of chemically induced permittivity changes caused by permanent and induced dipole moments at the NPL-ligand, inorganic−organic hybrid interface, resulting in the modulation of LSPR properties, specifically increasing the absorption coefficient values. Most importantly, we have determined that ligands containing a strong binding head group along with an electron-donating ability are ideal ligands for passivating the surface and enhancing optoelectronic properties. Furthermore, thin films comprising WO_{3-x} NPLs were analyzed by spectroscopic ellipsometry to determine the complex dielectric functions, which confirms the existence of the strong LSPR response of thin films. As a proof of concept, we have analyzed the photochromic response of these spin-coated thin films. Taken together, the fundamental study delineating the interfacial electronic effects on LSPR and dielectric properties of ligand-passivated WO_{3-x} NPLs would expect to broaden the field of plasmonics and expedite photochromic smart window and optical switch fabrication utilizing LSPR-active, less expensive metal oxide NCs.

EXPERIMENTAL SECTION

Materials. Tungsten (V) ethoxide was purchased from Alfa Aesar. Myristic acid (MA, ≥99%), 1-octadecene (ODE, 90%), oleylamine (OLA, 70%), tetradecylphosphonic acid (TD-PA, 98%), ethylphosphonic acid (Ethyl-PA, 98%), phenylphosphonic acid (Phenyl-PA, 98%), and 4-nitrobenzoic acid (NO_2-BA, 98%), were purchased from Sigma-Aldrich. Chloroform (99.9%), toluene (99.9%), and ethanol (99%) were purchased from Fisher Scientific. All chemicals were used without further purification unless otherwise noted in the synthesis procedure.

Synthesis, Ligand Treatment, and Purification of LSPR-active WO_{3-x} NPLs. Standard Schlenk line techniques were used to synthesize WO_{3-x} NPLs. For this, 0.513 g of (2.25 mmol) MA and 5.0 mL of 1-ODE were mixed in a 50 mL 3-neck round bottom flask and purged with N_2 at 125 °C for 30 min, and then degassed for another 1.5 h. The temperature of the reaction mixture was then raised to 290 °C and then 0.17 mmol (70 μL) of tungsten (V) ethoxide was quickly injected. Immediately, an N_2 purged solution of

https://doi.org/10.1021/acsanm.2c02218
ACS Appl. Nano Mater. 2022, 5, 9970−9980

0.5 mL of 1-ODE and 0.5 mL of (1.5 mmol) OLA was injected and the reaction was stirred for 1 h at 290 °C under N_2. The reaction was allowed to cool to 100 °C, and the solution was transferred to a N_2 purged 3-neck 50 mL round bottom flask containing 0.4 mmol of the desired ligand (TD-PA, Phenyl-PA, Ethyl-PA). We used 3.0 mmol of NO_2-BA to drive the ligand exchange. The temperature of the reaction mixture containing WO_{3-x} NPLs and ligands was raised to 140 °C and stirred for an additional 1 h. The reaction was removed from the heat and allowed to cool to room temperature. At this point, 5.0 mL of $CHCl_3$ was added to the flask and transferred to a 50 mL centrifuge tube. Then, 20 mL of ethanol was added to form a solid precipitate, which was collected by centrifugation at 10 000 rpm for 10 min.

Film Fabrication via Spin Coating. Ligand-passivated WO_{3-x} NPLs were redispersed in a 1-mL 50:50 mixture of chloroform:toluene. The NPL films were prepared on either 15 mm × 15 mm piranha cleaned glass microscope slides or silicon wafers. A 0.2 mL solution of ligand-passivated WO_{3-x} NPLs was spin coated onto the substrate first by dewetting at 500 rpm for 20 s followed by drying at 2000 rpm for 1 min. All films were then stored under a N_2 environment for further spectroscopy and microscopy characterizations.

Microscopy and Spectroscopy Characterizations. *XRD Analysis.* Diffraction patterns were recorded on a Bruker D8 Discover X-ray diffractometer (Cu Kα, λ = 1.54 Å) using a 2D VÅNTEC-500 detector from 5−60° 2θ with 5° 2θ steps and 30 s per step. All steps were then combined and integrated to obtain one one-dimensional diffraction pattern.

TEM Analysis. A Tecnai G2 12 Bio Twin instrument equipped with an AMT CCD camera operating at 120 kV was used to acquire TEM images. A 10 μL chloroform dispersion of NPLs was dropcast on carbon-coated copper TEM grids (Electron Microscopy Sciences). Excess solvent was wicked away with filter paper after 10 s.

AFM Analysis. Surface topography was acquired using a Nanosurf Naio AFM in the phase-contrast mode. All of the samples were measured with a constant setpoint for a 1 μm × 1 μm area. An automatic PID feedback loop along with an active noise reduction platform resulted in noise-free data acquisition. Measurements were performed on various spots to generate an average roughness value. Post-measurement analysis was performed using open-source WSXM software.

SEM Analysis. Film thickness and top-view images were obtained using a JEOL 7800f field-emission SEM with an acceleration voltage of 15 keV.

UV−vis-NIR absorbance/transmission spectra were recorded with a Perkin Elmer Lambda 19 UV/Visible/NIR spectrometer by taping NPLs thin films on glass substrates. All spectra were recorded from 300 to 3000 nm.

FTIR Analysis. All spectra were recorded in the transmission mode using a Thermo Scientific Nicolet iS10 spectrometer with Omnic 8.2 software. Samples were dispersed in $CHCl_3$ and placed onto a 4 mm KBr plate and solvent was allowed to evaporate in a vacuum oven at 60 °C, and then 100 data acquisition was used to record spectra.

Raman Spectroscopy. NPLs films on silicon substrates were used to acquire spectra using a XploRA Plus Raman microscope from Horiba Scientific. Spectra were obtained using a 583 nm laser at 25% power, 1800 line/mm grating and 10× objective. An acquisition time of 5 s was used with 5 accumulations.

Ellipsometry. The WO_{3-x} NPL thin films, passivated with different functional molecules, were probed with spectroscopic ellipsometry technique to extract wavelength-dependent optical constants. A Semilab SE-2000 was employed to collect Ψ (azimuth) and Δ (phase) values from the visible to mid-NIR region (400−1600 nm) with an optical resolution of 2 nm. The photon incident angle was kept at 75°, which is very close to the Brewster angle of the Si wafer. The sample was kept at 300 K under atmospheric conditions. The measured data were further processed in an Ellipsometry Analyzer v1.6.6.2 to extract various optical constants. The measured Ψ and Δ were fitted with an appropriate optical model to extract the real and imaginary part of permittivity of as-coated thin films. Except for the Ethyl-PA-passivated WO_{3-x} NPL thin film, other films were fitted with the Drude dispersion model. The accuracy of optical data fitting was more than 99% for all samples.

Density Functional Theory Calculations of W-ligand complexes. For the calculations of dipole moment and polarizability, first-principles density functional theory (DFT) calculation was carried out for each of the free ligand systems with and without the WO_{3-x} cluster model at the BP86 and B3LYP functional levels, respectively, in the Gaussian 16 program.[62] The LANL2DZ basis set was used for the W atom and the 6−311 + G(d,p) basis set for the other atoms. The optimized structures were visualized using Gaussview.[63]

Photochromic Study of Ligand-Passivated WO_{3-x} NPL Films. Thin films fabricated on a 15 mm × 15 mm glass slide were held in place approximately 2 cm from a Kessil LED Photo-Reaction Lighting PR160L (370 nm) light source. According to the intensity maps given by the manufacturer, this equates to an intensity of about 160 mW/cm^2. The power setting on the lamp was set to 75% power. The sample was irradiated for 5 min. Irradiated samples were immediately placed in a cuvette and LSPR spectra were collected from 820 to 2500 nm at 960 nm/min using an UV−vis−NIR spectrophotometer. For a particular sample, spectra were recorded every 3 min up to 30 min from the time of irradiation time and spectra were recorded every hour until 8 h. During the entire 8 h of study, samples were not moved from the instrument to avoid any additional light excitation.

■ ASSOCIATED CONTENT

Supporting Information

The Supporting Information is available free of charge at https://pubs.acs.org/doi/10.1021/acsanm.2c02218.

Optical results for the N_e value calculations, SEM images and cross-section images of photochromic films, energy minimized structure of meta−ligand complexes used for DFT calculations, time-dependent UV−vis-NIR spectra of ligand-passivated NPL films, and a table presenting DFT-calculated induced dipole moment values for metal−ligand complexes (PDF)

(PDF)

■ AUTHOR INFORMATION

Corresponding Authors

C. V. Ramana − *Department of Mechanical Engineering, University of Texas at El Paso, El Paso, Texas 79968, United States;* orcid.org/0000-0002-5286-3065; Email: rvchintalapalle@utep.edu

Rajesh Sardar − *Department of Chemistry and Chemical Biology, Indiana University-Purdue University-Indianapolis, Indianapolis, Indiana 46202, United States;* orcid.org/0000-0001-9680-1301; Email: rsardar@iupui.edu

Authors

Jacob T. Lee − *Department of Chemistry and Chemical Biology, Indiana University-Purdue University-Indianapolis, Indianapolis, Indiana 46202, United States*

Debabrata Das − *Department of Mechanical Engineering, University of Texas at El Paso, El Paso, Texas 79968, United States;* orcid.org/0000-0003-4326-6805

Gregory A. Davis, Jr. − *Department of Chemistry and Chemical Biology, Indiana University-Purdue University-Indianapolis, Indianapolis, Indiana 46202, United States*

Sumon Hati − *Department of Chemistry and Chemical Biology, Indiana University-Purdue University-Indianapolis, Indianapolis, Indiana 46202, United States;* orcid.org/0000-0002-4165-8314

https://doi.org/10.1021/acsanm.2c02218
ACS Appl. Nano Mater. 2022, 5, 9970−9980

Complete contact information is available at:
https://pubs.acs.org/10.1021/acsanm.2c02218

Author Contributions

[§]J.T.L. and D.D. contributed equally to this work. J.T.L. and R.S. conceived the original idea. J.T.L. conducted TEM, SEM, Raman, FTIR, and XRD analyses and UV-vis-NIR characterizations of thin films. D.D. and C.V.R. conducted AFM and ellipsometry analyses. G.A.D. performed photochromic studies and data analysis. S.H. conducted DFT calculations. The manuscript was written through contributions of all authors. All authors have given approval to the final version of the manuscript.

Notes

The authors declare no competing financial interest.
Additional SEM images, tables for free electron density and permittivity calculations, and structures used for permittivity.

■ ACKNOWLEDGMENTS

J.T.L., G.A.D., S.H., and R.S. thank the National Science Foundation grant (DMR-1747582) for supporting this work. C.V.R and D.D. acknowledge support from the National Science Foundation grant #DMR-1827745. RS also thanks the National Institute of Justice grant 2018-75-CX-0034 for the acquisition of a Raman microscope.

■ REFERENCES

(1) Narayanan, R.; El-Sayed, M. A. Catalysis with Transition Metal Nanoparticles in Colloidal Solution: Nanoparticle Shape Dependence and Stability. *J. Phys. Chem. B* **2005**, *109*, 12663−12676.
(2) Liang, X.; Bai, S.; Wang, X.; Dai, X.; Gao, F.; Sun, B.; Ning, Z.; Ye, Z.; Jin, Y. Colloidal Metal Oxide Nanocrystals as Charge Transporting Layers for Solution-Processed Light-Emitting Diodes and Solar Cells. *Chem. Soc. Rev.* **2017**, *46*, 1730−1759.
(3) Zhang, J.; Averitt, R. D. Dynamics and Control in Complex Transition Metal Oxides. *Annu. Rev. Mater. Res.* **2014**, *44*, 19−43.
(4) Sun, Y.; Chen, G.; Xi, S.; Xu, Z. J. Catalytically Influential Features in Transition Metal Oxides. *ACS Catal.* **2021**, *11*, 13947−13954.
(5) Agnihotri, A. S.; Varghese, A.; M, N. Transition Metal Oxides in Electrochemical and Bio Sensing: A State-of-Art Review. *Appl. Surf. Sci. Adv.* **2021**, *4*, No. 100072.
(6) Wang, S.; Fan, W.; Liu, Z.; Yu, A.; Jiang, X. Advances on Tungsten Oxide Based Photochromic Materials: Strategies to Improve Their Photochromic Properties. *J. Mater. Chem. C* **2018**, *6*, 191−212.
(7) Kalinin, S. V.; Spaldin, N. A. Functional Ion Defects in Transition Metal Oxides. *Science* **2013**, *341*, 858−859.
(8) Kreibig, U.; Vollmer, M. *Optical Properties of Metal Clusters*, 1st ed.; Springer-Verlag Berlin Heidelberg: Berlin, Heidelberg, 1995.
(9) Lee, S. A.; Link, S. Chemical Interface Damping of Surface Plasmon Resonances. *Acc. Chem. Res.* **2021**, *54*, 1950−1960.
(10) Zijlstra, P.; Paulo, P. M. R.; Yu, K.; Xu, Q.-H.; Orrit, M. Chemical Interface Damping in Single Gold Nanorods and Its near Elimination by Tip-Specific Functionalization. *Angew. Chem., Int. Ed.* **2012**, *51*, 8352−8355.
(11) Liyanage, T.; Nagaraju, M.; Johnson, M.; Muhoberac, B. B.; Sardar, R. Reversible Tuning of the Plasmoelectric Effect in Noble Metal Nanostructures through Manipulation of Organic Ligand Energy Levels. *Nano Lett.* **2020**, *20*, 192−200.
(12) Deb, S. K. Optical and Photoelectric Properties and Colour Centres in Thin Films of Tungsten Oxide. *Philos. Mag.* **1973**, *27*, 801−822.
(13) Deepa, M.; Srivastava, A. K.; Sood, K. N.; Agnihotry, S. A. Nanostructured Mesoporous Tungsten Oxide Films with Fast Kinetics for Electrochromic Smart Windows. *Nanotechnology* **2006**, *17*, 2625−2630.
(14) Balaji, S.; Djaoued, Y.; Albert, A.-S.; Brüning, R.; Beaudoin, N.; Robichaud, J. Porous Orthorhombic Tungsten Oxide Thin Films: Synthesis, Characterization, and Application in Electrochromic and Photochromic Devices. *J. Mater. Chem.* **2011**, *21*, 3940−3948.
(15) Azens, A.; Granqvist, C. Electrochromic Smart Windows: Energy Efficiency and Device Aspects. *J. Solid State Electrochem.* **2003**, *7*, 64−68.
(16) Qian, K.; Cai, G.; Nguyen, V. C.; Chen, T.; Lee, P. S. Direct Observation of Conducting Filaments in Tungsten Oxide Based Transparent Resistive Switching Memory. *ACS Appl. Mater. Interfaces* **2016**, *8*, 27885−27891.
(17) Vemuri, R. S.; Bharathi, K. K.; Gullapalli, S. K.; Ramana, C. V. Effect of Structure and Size on the Electrical Properties of Nanocrystalline WO_3 Films. *ACS Appl. Mater. Interfaces* **2010**, *2*, 2623−2628.
(18) Cong, S.; Geng, F.; Zhao, Z. Tungsten Oxide Materials for Optoelectronic Applications. *Adv. Mater.* **2016**, *28*, 10518−10528.
(19) Manthiram, K.; Alivisatos, A. P. Tunable Localized Surface Plasmon Resonances in Tungsten Oxide Nanocrystals. *J. Am. Chem. Soc.* **2012**, *134*, 3995−3998.
(20) Salje, E.; Güttler, B. Anderson Transition and Intermediate Polaron Formation in WO_{3-x} Transport Properties and Optical Absorption. *Philos. Mag. B* **1984**, *50*, 607−620.
(21) Niklasson, G. A.; Berggren, L.; Larsson, A.-L. Electrochromic Tungsten Oxide: The Role of Defects. *Sol. Energy Mater. Sol. Cells* **2004**, *84*, 315−328.
(22) Yu, W.; Shen, Z.; Peng, F.; Lu, Y.; Ge, M.; Fu, X.; Sun, Y.; Chen, X.; Dai, N. Improving Gas Sensing Performance by Oxygen Vacancies in Sub-Stoichiometric WO_{3-X}. *RSC Adv.* **2019**, *9*, 7723−7728.
(23) Paik, T.; Cargnello, M.; Godron, T. R.; Zhang, S.; Yun, H.; Lee, J. D.; Woo, H. Y.; Oh, S. J.; Kagan, C. R.; Fornaskero, P.; Murray, C. B. Photocatalytic Hydrogen Evolution from Substoichiometric Colloidal WO_{3-X} Nanowires. *ACS Energy Lett.* **2018**, *3*, 1904−1910.
(24) Li, Y.-Y.; Zhong, C.-Y.; Li, M.-X.; Zhang, Q.-Y.; Chen, Y.; Liu, Z.-Q.; Zhang, J. Z. Tuning Morphology-Dependent Localized Surface Plasmon Resonance in Quasi-Metallic Tungsten Oxide Nanostructures for Enhanced Photocatalysis. *J. Mater. Chem. C* **2021**, *9*, 1614−1621.
(25) Tang, H.; Tang, Z.; Bright, J.; Liu, B.; Wang, X.; Meng, G.; Wu, N. Visible-Light Localized Surface Plasmon Resonance of WO_{3-X} Nanosheets and Its Photocatalysis Driven by Plasmonic Hot Carriers. *ACS Sustainable Chem. Eng.* **2021**, *9*, 1500−1506.
(26) Prusty, G.; Lee, J. T.; Seifert, S.; Muhoberac, B. B.; Sardar, R. Ultrathin Plasmonic Tungsten Oxide Quantum Wells with Controllable Free Carrier Densities. *J. Am. Chem. Soc.* **2020**, *142*, 5938−5942.
(27) Heo, S.; Dahlman, C. J.; Staller, C. M.; Jiang, T.; Dolocan, A.; Korgel, B. A.; Milliron, D. J. Enhanced Coloration Efficiency of Electrochromic Tungsten Oxide Nanorods by Site Selective Occupation of Sodium Ions. *Nano Lett.* **2020**, *20*, 2072−2079.
(28) Wang, Z.; Gong, W.; Wang, X.; Chen, Z.; Chen, J.; Sun, H.; Song, G.; Cong, S.; Geng, F.; Zhao, Z. Remarkable near-Infrared Electrochromism in Tungsten Oxide Driven by Interlayer Water-Induced Battery-to-Pseudocapacitor Transition. *ACS Appl. Mater. Interfaces* **2020**, *12*, 33917−33925.
(29) Baetens, R.; Jelle, B. P.; Gustavsen, A. Properties, Requirements and Possibilities of Smart Windows for Dynamic Daylight and Solar Energy Control in Buildings: A State-of-the-Art Review. *Sol. Energy Mater. Sol. Cells* **2010**, *94*, 87−105.
(30) Lee, J. T.; Hati, S.; Fahey, M. M.; Zaleski, J. M.; Sardar, R. Surface-Ligand-Controlled Enhancement of Carrier Density in Plasmonic Tungsten Oxide Nanocrystals: Spectroscopic Observation of Trap-State Passivation Via Multidentate Metal Phosphonate Bonding. *Chem. Mater.* **2022**, *34*, 3053−3066.
(31) Ramana, C. V.; Baghmar, G.; Rubio, E. J.; Hernandez, M. J. Optical Constants of Amorphous, Transparent Titanium-Doped

Tungsten Oxide Thin Films. *ACS Appl. Mater. Interfaces* **2013**, *5*, 4659−4666.
(32) Paniagua, S. A.; Giordano, A. J.; Smith, O. N. L.; Barlow, S.; Li, H.; Armstrong, N. R.; Pemberton, J. E.; Brédas, J.-L.; Ginger, D.; Marder, S. R. Phosphonic Acids for Interfacial Engineering of Transparent Conductive Oxides. *Chem. Rev.* **2016**, *116*, 7117−7158.
(33) Davidowski, S. K.; Lisowski, C. E.; Yarger, J. L. Characterizing Mixed Phosphonic Acid Ligand Capping on CdSe/ZnS Quantum Dots Using Ligand Exchange and NMR Spectroscopy. *Magn. Reson. Chem.* **2016**, *54*, 234−238.
(34) Salje, E.; Carley, A. F.; Roberts, M. W. The Effect of Reduction and Temperature on the Electronic Core Levels of Tungsten and Molybdenum in WO_3 and $W_xMo_{1-X}O_{3-a}$ Photoelectron Spectroscopic Study. *J. Solid State Chem.* **1979**, *29*, 237−251.
(35) Lu, C.; Li, J.; Yan, J.; Li, B.; Huang, B.; Lou, Z. Surface Plasmon Resonance and Defects on Tungsten Oxides Synergistically Boost High-Selective CO_2 Reduction for Ethylene. *Appl. Mater. Today* **2020**, *20*, No. 100744.
(36) Zandi, O.; Agrawal, A.; Shearer, A. B.; Reimnitz, L. C.; Dahlman, C. J.; Staller, C. M.; Milliron, D. J. Impacts of Surface Depletion on the Plasmonic Properties of Doped Semiconductor Nanocrystals. *Nat. Mater.* **2018**, *17*, 710−717.
(37) Agrawal, A.; Cho, S. H.; Zandi, O.; Ghosh, S.; Johns, R. W.; Milliron, D. J. Localized Surface Plasmon Resonance in Semiconductor Nanocrystals. *Chem. Rev.* **2018**, *118*, 3121−3207.
(38) Leng, X.; Pereiro, J.; Strle, J.; Dubuis, G.; Bollinger, A. T.; Gozar, A.; Wu, J.; Litombe, N.; Panagopoulos, C.; Pavuna, D.; Božović, I. Insulator to Metal Transition in WO_3 Induced by Electrolyte Gating. *npj Quantum Mater.* **2017**, *2*, No. 35.
(39) Andron, I.; Marichez, L.; Jubera, V.; Fargues, A.; Frayret, C.; Gaudon, M. Improvement of the Photochromism Taking Place on ZnO/MoO_3 Combined Material Interfaces. *Mater. Adv.* **2021**, *2*, 782−792.
(40) Bronstein, L. M.; Huang, X.; Retrum, J.; Schmucker, A.; Pink, M.; Stein, B. D.; Dragnea, B. Influence of Iron Oleate Complex Structure on Iron Oxide Nanoparticle Formation. *Chem. Mater.* **2007**, *19*, 3624−3632.
(41) Lambert, J. B.; Gronert, S.; Shurvell, H. F.; Lightner, D. A. *Organic Structural Spectroscopy*, 2nd ed.; Pearson Prentice Hall: United States, 2011.
(42) Farrell, Z. J.; Reger, N.; Anderson, I.; Gawalt, E.; Tabor, C. Route to Universally Tailorable Room-Temperature Liquid Metal Colloids Via Phosphonic Acid Functionalization. *J. Phys. Chem. C* **2018**, *122*, 26393−26400.
(43) Seip, C. T.; Granroth, G. E.; Meisel, M. W.; Talham, D. R. Langmuir−Blodgett Films of Known Layered Solids: Preparation and Structural Properties of Octadecylphosphonate Bilayers with Divalent Metals and Characterization of a Magnetic Langmuir−Blodgett Film. *J. Am. Chem. Soc.* **1997**, *119*, 7084−7094.
(44) Heo, S.; Kim, J.; Ong, G. K.; Milliron, D. J. Template-Free Mesoporous Electrochromic Films on Flexible Substrates from Tungsten Oxide Nanorods. *Nano Lett.* **2017**, *17*, 5756−5761.
(45) Tilley, R. J. D. The Crystal Chemistry of the Higher Tungsten Oxides. *Int. J. Refract. Met. Hard Mater.* **1995**, *13*, 93−109.
(46) Escalante, G.; López, R.; Demesa, F. N.; Villa-Sánchez, G.; Castrejón-Sánchez, V. H.; de la Cruz, I. V. Correlation between Raman Spectra and Color of Tungsten Trioxide (WO_3) Thermally Evaporated from a Tungsten Filament. *AIP Adv.* **2021**, *11*, No. 055103.
(47) Houweling, Z. S.; Geus, J. W.; de Jong, M.; Harks, P.-P. R. M. L.; van der Werf, K. H. M.; Schropp, R. E. I. Growth Process Conditions of Tungsten Oxide Thin Films Using Hot-Wire Chemical Vapor Deposition. *Mater. Chem. Phys.* **2011**, *131*, 375−386.
(48) Chen, S.; Xiao, Y.; Xie, W.; Wang, Y.; Hu, Z.; Zhang, W.; Zhao, H. Facile Strategy for Synthesizing Non-Stoichiometric Monoclinic Structured Tungsten Trioxide ($WO_{(3-X)}$) with Plasma Resonance Absorption and Enhanced Photocatalytic Activity. *Nanomaterials* **2018**, *8*, No. 553.
(49) Sarycheva, A.; Gogotsi, Y. Raman Spectroscopy Analysis of the Structure and Surface Chemistry of $Ti_3C_2T_x$ Mxene. *Chem. Mater.* **2020**, *32*, 3480−3488.
(50) Chen, X.; Zhou, Y.; Liu, Q.; Li, Z.; Liu, J.; Zou, Z. Ultrathin, Single-Crystal WO_3 Nanosheets by Two-Dimensional Oriented Attachment toward Enhanced Photocatalystic Reduction of CO_2 into Hydrocarbon Fuels under Visible Light. *ACS Appl. Mater. Interfaces* **2012**, *4*, 3372−3377.
(51) Saito, N.; Ryuzaki, S.; Tsuji, Y.; Noguchi, Y.; Matsuda, R.; Wang, P.; Tanaka, D.; Arima, Y.; Okamoto, K.; Yoshizawa, K.; Tamada, K. Effect of Chemically Induced Permittivity Changes on the Plasmonic Properties of Metal Nanoparticles. *Commun. Mater.* **2021**, *2*, No. 54.
(52) Foerster, B.; Spata, V. A.; Carter, E. A.; Sönnichsen, C.; Link, S. Plasmon Damping Depends on the Chemical Nature of the Nanoparticle Interface. *Sci. Adv.* **2019**, *5*, No. eaav0704.
(53) Ye, X.; Fei, J.; Diroll, B. T.; Paik, T.; Murray, C. B. Expanding the Spectral Tunability of Plasmonic Resonances in Doped Metal-Oxide Nanocrystals through Cooperative Cation−Anion Codoping. *J. Am. Chem. Soc.* **2014**, *136*, 11680−11686.
(54) Bourdin, M.; Salek, G.; Fargues, A.; Messaddeq, S.; Messaddeq, Y.; Cardinal, T.; Gaudon, M. Investigation on the Coloring and Bleaching Processes of WO_{3-X} Photochromic Thin Films. *J. Mater. Chem. C* **2020**, *8*, 9410−9421.
(55) Deb, S. K. Opportunities and Challenges in Science and Technology of WO_3 for Electrochromic and Related Applications. *Sol. Energy Mater. Sol. Cells* **2008**, *92*, 245−258.
(56) Wei, J.; Jiao, X.; Wang, T.; Chen, D. The Fast and Reversible Intrinsic Photochromic Response of Hydrated Tungsten Oxide Nanosheets. *J. Mater. Chem. C* **2015**, *3*, 7597−7603.
(57) Evdokimova, O. L.; Kusova, T. V.; Ivanova, O. S.; Shcherbakov, A. B.; Yorov, K. E.; Baranchikov, A. E.; Agafonov, A. V.; Ivanov, V. K. Highly Reversible Photochromism in Composite WO_3/Nanocellulose Films. *Cellulose* **2019**, *26*, 9095−9105.
(58) He, T.; Ma, Y.; Cao, Y.; Hu, X.; Liu, H.; Zhang, G.; Yang, W.; Yao, J. Photochromism of WO_3 Colloids Combined with TiO_2 Nanoparticles. *J. Phys. Chem. B* **2002**, *106*, 12670−12676.
(59) Teunis, M. B.; Dolai, S.; Sardar, R. Effects of Surface-Passivating Ligands and Ultrasmall CdSe Nanocrystal Size on the Delocalization of Exciton Confinement. *Langmuir* **2014**, *30*, 7851−7858.
(60) Teunis, M. B.; Nagaraju, M.; Dutta, P.; Pu, J.; Muhoberac, B. B.; Sardar, R.; Agarwal, M. Elucidating the Role of Surface Passivating Ligand Structural Parameters in Hole Wave Function Delocalization in Semiconductor Cluster Molecules. *Nanoscale* **2017**, *9*, 14127−14138.
(61) *Handbook of Inorganic Electrochromic Materials*, 1st ed.; Elsevier Science: New York, 1995; p 650.
(62) Frisch, M. J. T.; G W S, H. B.; Scuseria, G. E.; Robb, M. A.; Cheeseman, J. R.; Scalmani, G.; Barone, V.; Petersson, G. A.; Nakatsuji, H.; Li, X.; Caricato, M.; Marenich, A. V.; Bloino, J.; Janesko, B. G.; Gomperts, R.; Mennucci, B.; Hratchian, H. P.; Ortiz, J. V.; Izmaylov, A. F.; Sonnenberg, J. L.; Williams-Young, D.; Ding, F.; Lipparini, F.; Egidi, F.; Goings, J.; Peng, B.; Petrone, A.; Henderson, T.; Ranasinghe, D.; Zakrzewski, V. G.; Gao, J.; Rega, N.; Zheng, G.; Liang, W.; Hada, M.; Ehara, M.; Toyota, K.; Fukuda, R.; Hasegawa, J.; Ishida, M.; Nakajima, T.; Honda, Y.; Kitao, O.; Nakai, H.; Vreven, T.; Throssell, K.; Montgomery, J. A., Jr.; Peralta, J. E.; Ogliaro, F.; Bearpark, M. J.; Heyd, J. J.; Brothers, E. N.; Kudin, K. N.; Staroverov, V. N.; Keith, T. A.; Kobayashi, R.; Normand, J.; Raghavachari, K.; Rendell, A. P.; Burant, J. C.; Iyengar, S. S.; Tomasi, J.; Cossi, M.; Millam, J. M.; Klene, M.; Adamo, C.; Cammi, R.; Ochterski, J. W.; Martin, R. L.; Morokuma, K.; Farkas, O.; Foresman, J. B.; Fox, D. J. *Gaussian 16*, revision C.01; Gaussian, Inc.: Wallingford, CT, 2016.
(63) Dennington, R. K.; T A M, J.M. *Gaussview*, Version 6; Semichem Inc.: Shawnee Mission, KS, 2016.

https://doi.org/10.1021/acsanm.2c02218
ACS Appl. Nano Mater. 2022, 5, 9970−9980